An innovative synthesis of carbon-coated TiO 2 nanoparticles as host for Na + intercalation for sodium-ion batteries

Tanguy Soudant, S. Fleutot, S. Bruyere, Lucie Speyer, Sebastien Hupont, Mickaël Bolmont, Thomas Girardet, Loris Raspado, Claire Hérold, Sébastien Cahen

Dalton Transactions

An international journal of inorganic chemistry

Accepted Manuscript

This article can be cited before page numbers have been issued, to do this please use: T. SOUDANT, S. Fleutot, S. Bruyère, L. Speyer, S. Hupont, M. Bolmont, T. Girardet, L. Raspado, C. Hérold and S. Cahen, *Dalton Trans.*, 2024, DOI: 10.1039/D4DT00459K.

ROYAL SOCIETY OF CHEMISTRY

rsc.li/dalton

View Article Online
DOI: 10.1039/D4DT00459K

ARTICLE

An innovative synthesis of carbon-coated TiO_2 nanoparticles as host for Na^+ intercalation for sodium-ion batteries

Received 00th January 20xx,
Accepted 00th January 20xx

DOI: 10.1039/x0xx00000x

Tanguy Soudant[a], Solenne Fleutot[a], Stéphanie Bruyère[a], Lucie Speyer[a], Sébastien Hupont[a], Mickaël Bolmont[a], Thomas Girardet[a], Loris Raspado[a], Claire Hérold[a], Sébastien Cahen[a]*

In this work, an innovative route to synthesize anatase TiO_2@C composite is presented. The synthesis was conducted by a soft chemistry microwave-assisted method using titanium(IV) butoxide as titanium precursor. The residual (un)converted titanum precursor remaining after TiO_2 synthesis was used as carbon precursor and thermally treated under H_2 to obtain nanoparticles of TiO_2@C composite. We showed a superior reversible specific capacity with TiO_2@C (120 mAh.g^{-1} at C/20 rate, 3rd cycle) than pristinne TiO_2 (66.5 mAh.g^{-1} at C/20 rate, 3rd cycle), in agreement with the importance of carbon coating addition with TiO_2 nanoparticles as negative electrode material for sodium-ion batteries.

Introduction

Currently, considering the environmental crisis, governments want to reduce greenhouse gas emissions. Therefore, electrification of the society is a way to free ourselves from fossil fuel. The corresponding technological changes cause a very important demand in energy storage devices especially for electric vehicles (full electric or hybrid). Indeed, in 2016 battery demand was around 41 to reach 550 GWh per year in 2022[1]. Nowadays, Li-ion batteries (LIBs) are widely used in mobile devices especially in electrical vehicles thanks to their high energy density storage. Among elements used for batteries, lithium, cobalt, nickel, copper and even carbon (graphite) will become critical elements in medium term (2025-2035) [2]. Moreover, lithium exploitation is not environmentally friendly, is it so necessary to develop sustainable alternatives for electrochemical storage technologies. Sodium-ion batteries (SIBs) appear as an interesting solution to free ourselves some critical elements cited previously. Unlike LIBs, graphite cannot be used as negative electrode material in SIBs due to poor sodium intercalation with very low theoretic massic capacity of 35 mAh.g^{-1} for NaC_{64} (372 mAh.g^{-1} for LiC_6)[3–5]. Consequently, hard carbons remain the most widely studied anode materials because there are very good candidates for sodium ion storage. It presents several advantages regarding the abundance of the carbon element, the low elaboration cost of hard carbons or its expected electrochemical performances (300mAh.g^{-1} for an energy density of 300 Wh.kg^{-1} for fully sodiated hard carbons [6–8]. Elsewhere, transition metal oxides are another possible class of anode materials and are considered for both LIBs and SIBs [9–11]. Among them, titanium dioxide (TiO_2) is an attractive alternative negative electrode material regarding the titanium abundance, its non-toxicity and the cost-effective of the material. Such anode could be envisaged in stationary application where high massic/volumic capacities are not requested. Another interest of titanium dioxide compared with hard carbons is the safety aspect of TiO_2 as anode as its mean nominal voltage is 0.7 versus 0.1-0.05 V (*vs.* Na^+/Na) [8], avoiding Na plating risk [12] with increased cyclability [13]. TiO_2 is a highly studied inorganic material due to its numerous applications in photocatalysis, cosmetic as white pigment, optics, sensors or rechargeable batteries[14]. Many polymorphs of TiO_2 exist but the most common phases are rutile (tetragonal, $P4_2/mnm$), brookite (orthorhombic, *Pbca*) and anatase (tetragonal, $I4_1/amd$). The anatase polymorph, thermodynamically stable at low temperature, is the most studied for batteries applications due to its easy synthesis and electrochemical stability [15–18]. Especially, anatase polymorph reveals the highest sodium storage [13,19,20] as described in Eq.1 where y corresponds to the number of inserted Na^+:

$$TiO_2 + yNa^+ + ye^- \leftrightarrow Na_yTiO_2 \qquad (Eq.1)$$

The nanoscale allows reaching better storage performance than macroscale due to reducing diffusion lengths, large specific surface area and high kinetic properties[21–23]. In the literature, Titanium NanoParticles (TNPs) are mostly synthetized by hydrothermal route[24,25]. In this work syntheses have been performed by a microwave-assisted procedure due to many advantages such as time gain, reducing power consumption, homogenous heat and smaller size particles obtaining compared to hydrothermal route[26]. Unfortunately, TNPs are electrochemically instable toward electrolyte due to a huge specific surface area that causes an important irreversible consumption of Na^+ during the formation of the Solid Electrolyte Interphase (SEI) at the electrode/electrolyte interface [19,27]. So many works are focused on the improvement

[a] Institut Jean Lamour, CNRS UMR 7198, Université de Lorraine, 54000 Nancy. France
* sebastien.cahen@univ-lorraine.fr

of the electrochemical stability of TNPs. Indeed, if three-dimensional TiO_2 anatase structure exhibit open galleries favourable for Na^+ insertion/deinsertion[28], it suffers from low conductivity and slow ion diffusion[29].

One cost-effective approach used for improving the capacity and rate capability is the formation carbon coating surrounding TNPs. A porous carbon matrix will bring preferential sites for Na+ insertion/deinsertion, improve the contact between active material and electrolyte by its penetration through pores and optimize conduction paths for fast electron transport [30,31].

It is expected that the carbon will add a synergetic effect, providing a conductive network that will also stabilize the SEI, improving the Initial Coulombic Efficiency together with increased capacity and rate performances. Indeed, it has been demonstrated that carbon coating allows improving the electronic conductivity of TNPs trough the formation of a Ti-C bond, contributing to better electrochemical performances[27,30]. To coat nanoparticles, many routes exist such as sol-gel[31,32], hydrothermal[33,34] or microwave-assisted[35] routes. In this work, In this work, we employed a one-pot TNPs synthesis followed by direct thermal treatment without adding supplementary reactant. This original approach is assumed to improve the TNPs stability using $Ti(OCH_2CH_2CH_2CH_3)_4$ (TetraButOxyTitanium TBOT) as both titanium and carbon precursors. To do so, as-prepared TNPs were thermally treated under H_2 flow.

Experimental

Synthesis of TiO_2@C nanoparticles

Usually, TiO_2 nanoparticles (TNPs) are mainly synthesized by hydrothermal route [24,25]. In this work, all syntheses have been conducted by microwave-assisted which allows energy and time gains compared to hydrothermal route[26]. To synthesize TNPs, samples are prepared in a glove bag under argon atmosphere to prevent hydrolysis of TBOT. 4 mL of TBOT (*Aldrich Chemistry, 97%, CAS: 5593-70-4*) and 8 mL of acetic acid (*Sigma Aldrich, ≥ 99.8%, CAS: 64-19-7*) are introduced into a microwave vial then transferred into a single-mode microwave (Monowave 400 from Anton Paar) for the thermal treatment at a temperature between 180 and 240 °C for 30 minutes and finally cooling at 55 °C. The reaction mechanisms involved can be described by the following reactions[36]:

$$Ti(OBu)_4 + 4H_2O \rightarrow Ti(OH)_4 + 4BuOH \qquad (Eq.2)$$

$$Ti(OH)_4 \rightarrow TiO_2 + 2H_2O \qquad (Eq\ 3)$$

The obtained mixture containing TiO_2 nanoparticles is then washed once with absolute ethanol (*VWR, 99.95%, CAS: 64-17-5*) and twice with ultra-pure water (resistivity: 18.2 MΩ.cm) by centrifugation for 5 minutes for each washing then dried at 80 °C. The TNPs powder with carbon precursor was loaded in a silica boat and thermally treated under H_2 flux (70 mL.min^{-1}) for 4h at 400 °C (5 °C.min^{-1}) in a horizontal furnace.

Characterizations

The TNPs phase was identified by powder X-ray diffraction (pXRD) using a Bruker diffractometer (D8 Advance) with Mo Kα radiation (0.70926 Å) in transmission mode and Cu Kα radiation (1.54060 Å) in reflexion mode (θ-θ geometry). Thermogravimetric analyses (Setaram - Setsys EV1750) coupled with mass spectroscopy (Pfeiffer Vacuum - Omnistar GSD 301C) were conducted at a heating rate of 5 °C.min^{-1} from room temperature to 800 °C and a cooling rate of 10 °C.min^{-1}. Carbon in the samples was evidenced by Raman spectroscopy using a Horiba spectrometer (Labram HR800) operating with a 457 nm wavelength. High-resolution transmission electron microscopy (HR-TEM) was performed (JEOL – ARM 200F) to study morphology, size, and crystallinity of particles. Scanning TEM (STEM) mode was used for chemical analysis by Electron Energy Loss Spectroscopy (EELS).

Electrochemical characterization

To perform electrochemical characterizations, a 70/10/20 slurry (70 wt% active material, 10 wt% carboxymethyl cellulose as binder and 20 wt% carbon black as conductive material) was prepared in deionized water and then coated on aluminium foil [37] . Once slurry has dried, the material was assembled on current collector in coin cell CR2032 or in powder in Swagelok® half-cell versus Na metallic foil us 1M $NaClO_4$ in EC-DMC 1:1 in mass. Galvanostatic Cycling with Potential Limitation (GCPL) tests were conducted on Biologic – BCS-810 between 0 and 3 V vs. Na^+/Na at C/20 rate.

Results and discussions

Effect of the synthesis temperature

To study the temperature influence on the TNPs crystallinity, four different synthesis temperatures were tested. On the XRD patterns shown in Fig. 1, the diffraction peaks can all be indexed with anatase TiO_2 only (COD n° 96-900-8216). FWHM of the peaks decreases from 0.3149 to 0.2558 for 101 reflection and from 0.6298 to 0.3149 for the 200 reflection when the temperature increases, which characterizes a higher crystallite size (from 16 nm for 180 °C to 27 nm for 240 °C, calculated by Scherrer equation from 101 peak). Moreover, a low angle background signal is detected due to the presence of residual

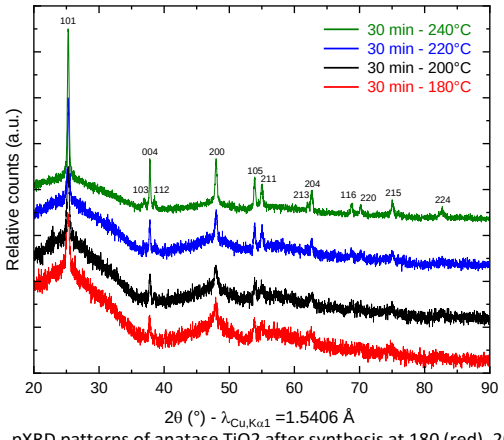

Fig. 1 pXRD patterns of anatase TiO2 after synthesis at 180 (red), 200 (black), 220 (blue) and 240 °C (green).

amorphous material. This background decreases progressively by increasing the temperature in agreement with the sharpening of the Bragg peaks accordingly to a higher crystallinity. Fig. 2 presents ThermoGravimetric Analyses (TGA) for the sample synthesized at 180 °C. This thermogram is considered as representative of all samples of the study (data retrieved from other ones are summarized in Table 1). Such an analysis allows quantifying the residual quantity of titanium precursor after synthesis. Two mass losses signals are present: the first one is attributed to H_2O outgassing at 45 °C and the second one to the combustion of residual TBOT at 318 °C. Whatever the temperature synthesis considered, the TBOT mass loss does not change, in agreement with a reaction yield close to 70 %.

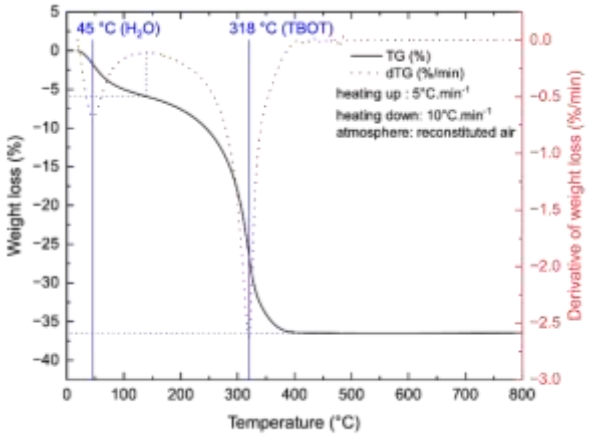

Fig. 2 TGA of TNPs after synthesis (180 °C – 30 min).

Thermal treatment

After synthesis, thermal treatment of TNPs under H_2-flux at 400 °C was carried out to remove TBOT residues and integrate TiO_2 into carbon. Indeed, residual TBOT present at around 30 $\%_{wt}$ is assumed to be usable as a carbon precursor to form the carbon coating. pXRD patterns (Fig. 3) are recorded before and after thermal treatment under H_2 using a diffractometer with Mo $K_{\alpha1}$ radiation in order to probe the sample in transmission mode. pXRD patterns show no-TiO_2 reduction into Ti, as thermodynamically expected up to 500 °C. It should be noted that TiO_2 polymorph is preserved, and the crystalline phase ratio is improved after thermal treatment. The SiO_2 reflection peak at 9.78 °(2θ) is attributed to the silica boat used

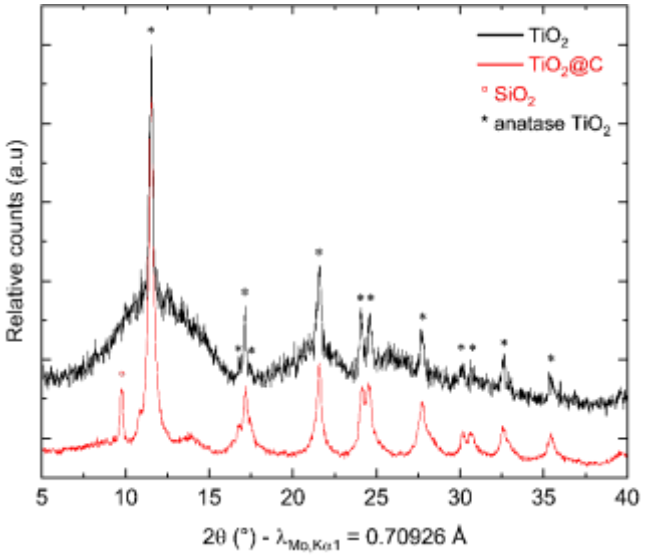

Fig. 3 pXRD patterns before (black) and after (red) heat treatment under H_2

for the thermal treatment. Finally, the splitting of the peak around 11 °(2θ) could be due to the 002 reflection of a poorly crystallized carbon. To confirm the presence of carbon after this step, TG-MS analysis was performed, and the results are presented in Fig. 4.

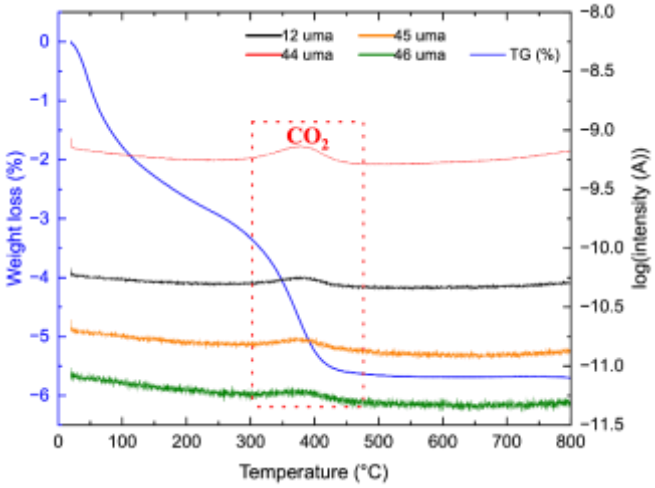

Fig. 4 TG-MS analysis under air of TNPs after thermal treatment.

The weight loss can be decomposed in two phenomena as previously observed. The first one at around 45 °C is still

Table 1 Quantitative data of TG analysis for the different synthesis temperatures.

Synthesis temperature (°C)	H_2O weight loss (%)	Weight loss temperature (°C)	TBOT weight loss (%)	Decomposition temperature (°C)
180	6	45	31	318
200	7	43	30	317
220	6	42	30	318
240	4	54	27	314

View Article Online
DOI: 10.1039/D4DT00459K

attributed to H_2O outgassing, and the second one at around 370 °C (higher than for pristine TiO_2 nanoparticles) is correlated with CO_2 detected by mass spectroscopy. This second weight loss can be assigned to the combustion of around 3 wt% of carbon. This carbon amount is in accordance with Devina *et al.* who obtained 0.2-4.1 wt% carbon depending on the carbon impregnation method[38]. The weak combustion temperature is probably due to the amorphous nature of the carbon material formed on the surface of the particles[39]. Complementary to mass spectroscopy, Raman spectroscopy is performed to evidence the obtaining of carbon. Indeed, it consists in a powerful tool to characterize carbon materials. Six active Raman vibration modes due to the D_{2d} local symmetry of anatase TiO_2 are observed on the spectrum (Fig. 5): $1A_g + 2B_{1g} + 3E_g$ [40,41] at range 100-750 cm^{-1} identified by purple zone.

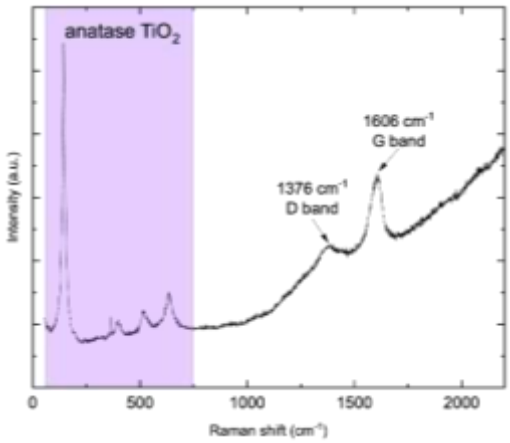

Fig.5 Raman spectrum of TiO_2@C (457 nm wavelength).

D and G bands respectively present at 1376 and 1606 cm^{-1} corroborate the presence of carbon material as revealed after TGA analysis. D band (disordered sp^2 carbon) is expected around 1350 cm^{-1} [31,42–45] but a shift is observed due to the excitation wavelength used [46]. Here I_D/I_G ratio is 0.22 but due to its parabolic evolution, it is not possible to conclude about carbon crystallinity. Indeed, as described by Merlen *et al.*, D band intensity increases with disorder, reaches a maximum and then, decreases when carbon being close to amorphous[47]. High-Resolution Transmission Electronic Microscopy (HR-TEM) was used to study carbon morphology. Selected Area Electron Diffraction (SAED) reveals diffraction plans of anatase TiO_2 (Table 2) in accordance with XRD measurement, and the good crystallinity of the particles. First TEM micrograph (Fig. 6 (a)) exhibits aggregated particles into an amorphous matrix. HR-TEM micrograph (Fig. 6 (b)) evidences atomic planes of the particles demonstrating titanium dioxide's crystallinity and allows to determine the size of the crystals, which is 8.5 ± 1.4 nm in accordance with XRD calculation. STEM-EDX elementary mapping images highlight the presence of carbon (Fig. 7). Thus, TG-MS, Raman spectroscopy and HR-TEM confirm the presence of carbon in samples thermally treated under H_2 using TBOT as a carbon precursor.

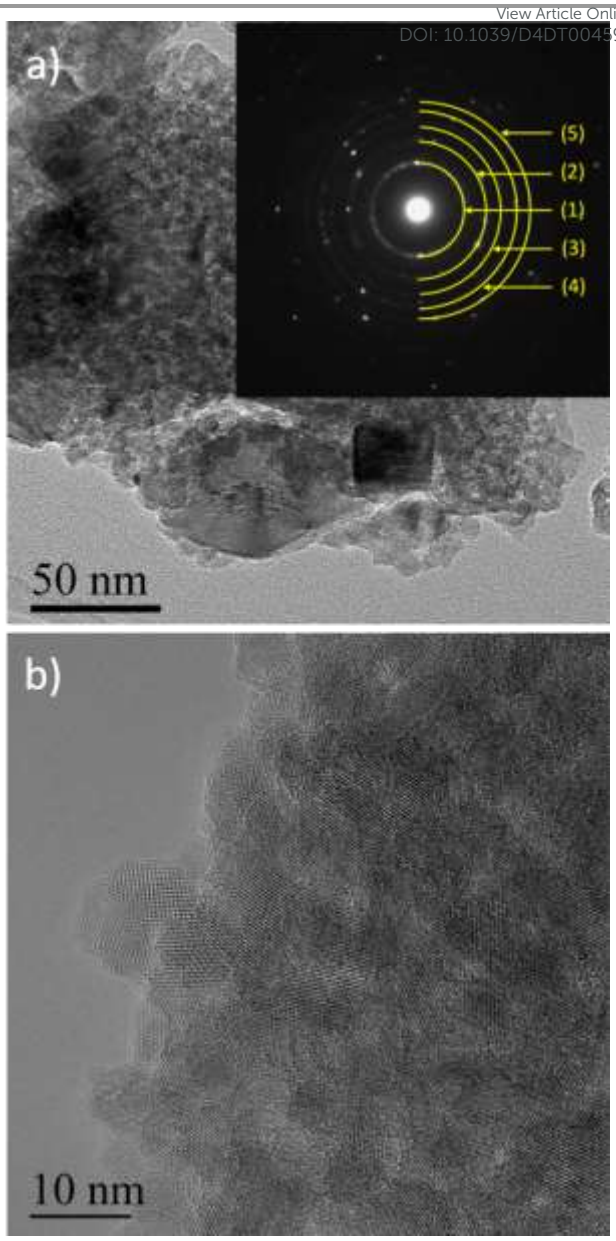

Fig. 6 BF-TEM with SAED a) and HR-TEM of TiO_2@C b).

Table 2 indexation from SAED.

Yellow half-circle (#)	d-spacing (nm)	(hkl)
(1)	0.3524	(101)
(2)	0.2394	(004)
(3)	0.1908	(200)
(4)	0.1711	(105)
(5)	0.1499	(213)

View Article Online
DOI: 10.1039/D4DT00459K

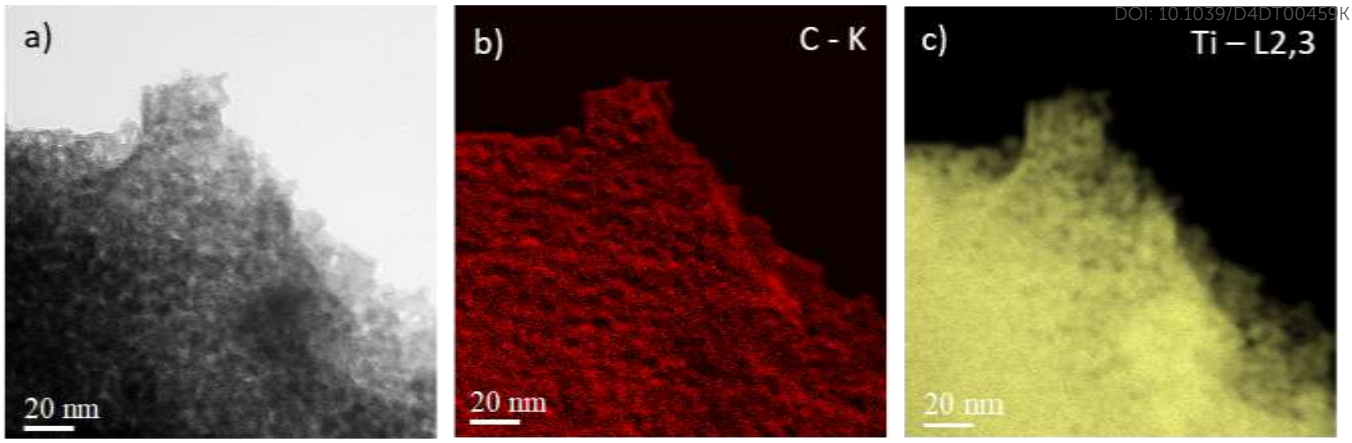

Fig. 7 BF-TEM a) and TEM elemental mapping images of carbon b) and titanium c) for TiO_2@C.

Electrochemical characterization

Pristine TiO_2

Galvanostatic curves of pristine TNPs (*i.e* without carbon), are presented Fig. 8. On the first discharge (sodiation) curve, three slopes can be noted ; the first one between 2 and 1.2 V vs. Na^+/Na, the second one between 1.2 and 0,25 V vs. Na^+/Na and the last one until 0 V vs. Na^+/Na. Wu *et al.* has described that the first one at high potential is related to a pseudo-capacitive

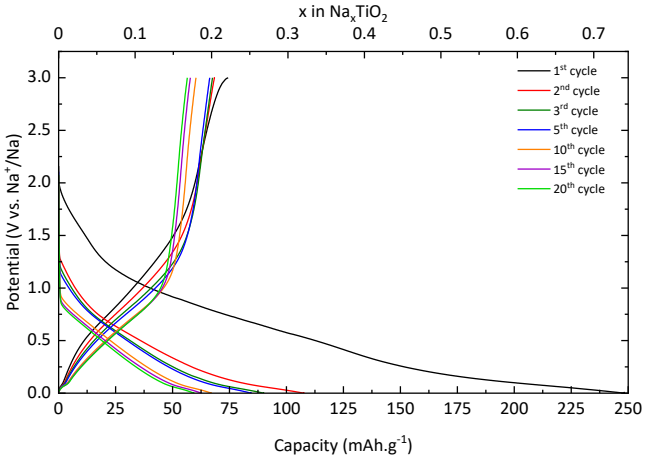

Fig. 8 charge/discharge curves of pristine TiO2 at C/20 rate.

process where no structural changes are observed [13]. Then, Na^+ insertion occurs with a structural transition and finally a disproportionation reaction with intermediate phase formation**.** The next cycles curves adopt a S-shape behaviour due to poor low crystallinity. First discharge curve indicates an intercalation of 0.75 Na^+ and a deintercalation of only 0.25 Na^+ into TiO_2 that corresponds to an irreversible capacity of 175 $mAh.g^{-1}$ and a reversible capacity of 75 $mAh.g^{-1}$. A fraction of Na^+ ions is continuously consumed to form the SEI, as shown by curves shift to lower capacity values, especially after the first cycle. At the 20th cycle, 0.18 Na^+ can be intercalated and 0.17 Na^+ are deintercalated. These results demonstrate the electrochemical instability of TiO_2 nanoparticles towards electrolyte (Fig. 8). The evolution of the capacity versus the number of cycles shows that the first irreversible capacity is significant, and the capacity continuously decreases (Fig. 9). At the first cycle, the columbic efficiency reaches 30 % due to SEI formation and reaches 95 % at 20th cycle that is an acceptable value for this kind of material and corresponds to results mentioned by Ge *et al.*[27]. Specific capacity goes down to 60 $mAh.g^{-1}$ at the 20th cycle, below the values mentioned in the literature[11,13,19,27,37]. The 30 % TBOT residues after the synthesis as electronic insulator can explain this result. Incremental dQ/dE versus E curves presented Fig. 10 allow determining the sodiation reaction potentials. In reduction path, the two peaks at 0.04 and 0.75 V vs. Na^+/Na corresponds to the sodiation reaction (Eq.4):

$$xNa^+ + xe^- + TiO_2 \rightarrow Na_xTiO_2 \qquad (Eq.4)$$

Desodiation reaction takes place at the same potential as sodiation reaction *i.e.* 0.75 V vs Na^+/Na (Eq.5):

$$Na_xTiO_2 \rightarrow xNa^+ + xe^- + TiO_2 \qquad (Eq.5)$$

In addition, the peaks at 0.04 V vs. Na^+/Na in reduction and 0.08 V vs. Na^+/Na are also attributed to electrolyte decomposition according to Wu *et al.*[13]. Finally, the signal between 1.3 and 0.9 V vs Na^+/Na that shifts to lower and lower potential values, is due to SEI formation, that corroborates results previously mentioned and demonstrates the electrochemical instability of TNPs toward electrolyte.

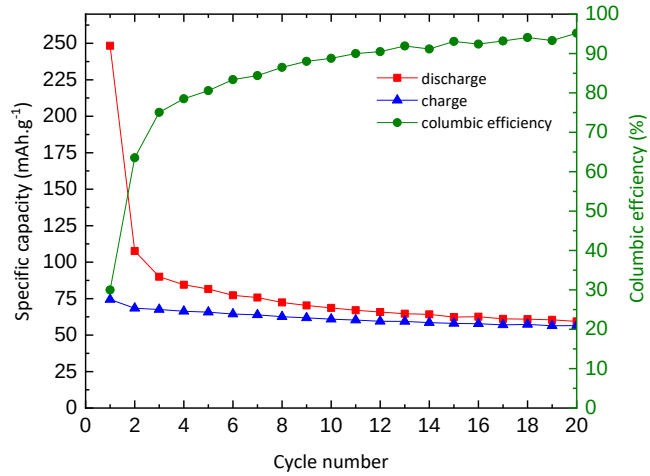

Fig. 9 evolution of charge (blue), discharge (red) capacities, and columbic efficiency (green) as function of the number of cycles.

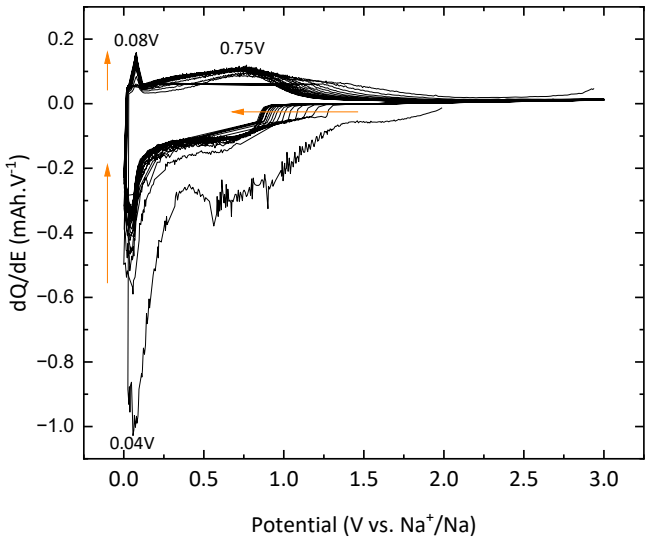

Fig. 10 dQ/dE curves of pristine TiO_2.

TiO_2@C

TNPs with carbon (TiO_2@C) were prepared as described in experimental section. As for pristine TiO_2, galvanostatic measurements measurements were used to characterize electrochemical properties of TNPs@C. On Fig. 11, the first discharge curve reveals a capacity of 220 $mAh.g^{-1}$ that corresponds to 0.65 intercalated Na^+, with a very long plateau at low potential and during the first charge, 0.33 Na^+ are deintercalated. At the 3rd cycle, the capacity reaches 115 $mAh.g^{-1}$, twice that of pristine TiO_2. Then, the capacity at the 20th cycle reaches 76 $mAh.g^{-11}$ (retention capacity of 67%), which is much higher than pristine TiO_2. Different values are summarized in Table 3. SEI formation seems to be reduced, demonstrating the stabilization of TNPs embedded in carbon compared to pristine TiO_2. Indeed, the initial coulombic efficiency at 1st cycle is 51% versus 30% for pristine TiO_2. Therefore, the carbon contribution to the stabilization and the improvement in electrochemical performances is significant.

The dQ/dE curve presented in Fig. 12 shows that sodium deinsertion (Eq. 4) takes place at a higher potential *i.e.* 0.9 V vs. Na^+/Na than pristine TiO_2 and the insertion mechanism (Eq. 5) occurs at 0.6 V vs. Na^+/Na which corresponds to the one mentioned by Ge *et al.*[27]. Moreover, electrolyte decomposition and sodium redox reactions still happen at low potential.

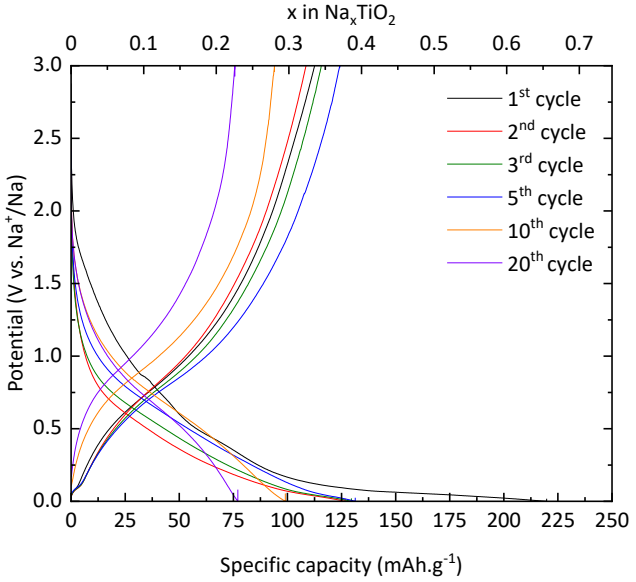

•**Fig. 11** charge/discharge curves of TiO_2@C.

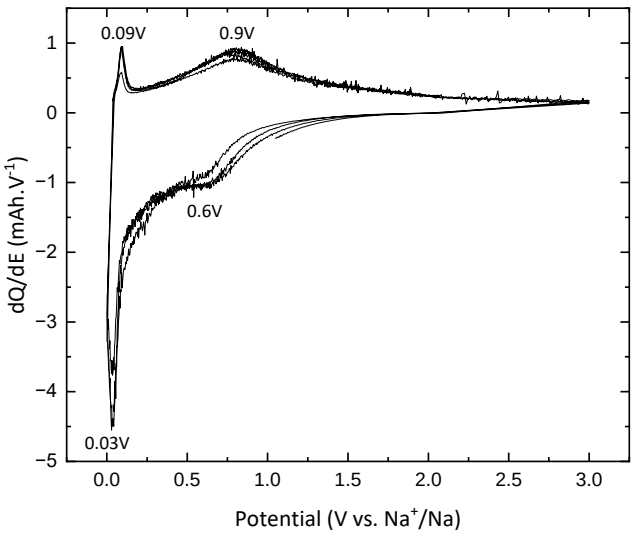

Fig. 12 dQ/dE curves of TiO@C.

Table 3 Summary of characteristic values.

Pristine TiO_2			
	Q discharge (mAh/g) - x_{Na}	Q charge (mAh/g) - x_{Na}	Efficiency (%)
Cycle 1	248.3 – 0.74	74.1 – 0.22	30
Cycle 3	90 – 0.27	67.5 – 0.20	75
Cycle 5	81.6 – 0.24	65.8 – 0.20	80.6
Cycle 10	68.6 – 0.20	60.9 – 0.18	88.8
Cycle 20	59.3 – 0.18	56.5 – 0.17	95.2
TiO_2@C			
	Q discharge (mAh/g) - x_{Na}	Q charge (mAh/g) - x_{Na}	Efficiency (%)
Cycle 1	219.8 – 0.65	112.6 – 0.34	51.2
Cycle 3	129.5 – 0.39	115.7 – 0.34	89.3
Cycle 5	131.3 – 0.39	124.2 – 0.37	94.6
Cycle 10	128.7 – 0.38	128.2 – 0.38	99.6
Cycle 20	77.1 – 0.23	75.7 – 0.22	98.2

Conclusions

Titanium dioxide nanoparticles were successfully obtained by microwave assisted method. TBOT residues were used as carbon precursor to prepare embedded carbon TNPs. TNPS@C exhibits electrochemical stabilization by improving efficiency during first cycle that corresponds to a decrease in the SEI formation. By carbon addition, capacity reached 115 $mAh.g^{-1}$ at the 3rd cycle against 67 $mAh.g^{-1}$ for pristine TNPs. Electrochemical performances of TiO_2@C presented in this work are still lower than those mentioned in other studies[11,31,48]. If our results are promising, with an ICE of only 51% and a capacity retention of 67%, the materials need further optimization (size and shape of TiO_2 nanoparticles; anchorage, thickness and porosity of the carbon matrix) before widespread commercialisation. The goal of this work is not the full optimization of the electrochemical performances and cycle life of TiO_2 as an anode for sodium-ion batteries, but mainly to bring a proof-of-concept for the innovative and simple synthesis of TiO_2@C intercalation material. Here, this work presents an original way for synthesizing TiO_2 nanoparticles by fast microwave assisted route. Moreover, it constitutes an advanced demonstration on the possibility to use one precursor as both Ti and C precursor. Nevertheless, an optimization of the TiO_2@C material can be considered on several points: control of the residual amorphous material after the microwave assisted step, morphology and crystallinity of TiO_2 anatase, carbon matrix optimization…

Moreover, the electrochemical stabilization of TiO_2 nanoparticles toward electrolyte thanks to carbon addition was proofed.

Author Contributions

Tanguy Soudant: Formal Analysis, Investigation, Writing Original Draft, Writing - Review & Editing, Visualization.
Solenne Fleutot: Conceptualization, Methodology, Validation, Investigation, Review & Editing, Visualization, Supervision
Stephanie Bruyère: Formal Analysis, Review & Editing
Lucie Speyer: Formal Analysis, Review & Editing
Mickaël Bolmont: Methodology, Review & Editing,
Thomas Girardet: Methodology, Review & Editing
Loris Raspasdo: Methodology, Review & Editing
Claire Hérold: Conceptualization, Writing - Review & Editing, Visualization
Sébastien Cahen: Conceptualization, Methodology, Validation, Formal Analysis, Resources, Writing - Review & Editing, Visualization, Funding acquisition, Supervision, Project administration

Conflicts of interest

There are no conflicts to declare.

Acknowledgements

The authors would like to thank the ORION program for its contribution to the funding of TS's research internship. This work has benefited from a French government grant managed by the Agence Nationale de la Recherche with the reference ANR-20-SFRI-0009.

Notes and references

1 Battery demand by region, 2016-2022 – Charts – Data & Statistics, https://www.iea.org/data-and-statistics/charts/battery-demand-by-region-2016-2022, (accessed January 24, 2024).
2 H. Kim, *ACS Mater. Au*, 2023, **3**, 571–575.
3 D. A. Stevens and J. R. Dahn, *Journal of The Electrochemical Society*, 2001, **148**, A803.
4 M. M. Doeff, Y. Ma, S. J. Visco and L. C. D. Jonghe, *Journal of The Electrochemical Society*, 1993, **140**, L169.
5 P. Ge and M. Fouletier, *Solid State Ion.*, 1988, **28–30**, 1172–1175.
6 V. Palomares, P. Serras, I. Villaluenga, K. B. Hueso, J. Carretero-González and T. Rojo, *Energy Environ. Sci.*, 2012, **5**, 5884.
7 S. Tan, H. Yang, Z. Zhang, X. Xu, Y. Xu, J. Zhou, X. Zhou, Z. Pan, X. Rao, Y. Gu, Z. Wang, Y. Wu, X. Liu and Y. Zhang, *Molecules*, 2023, **28**, 3134.
8 W. Lu, Z. Wang and S. Zhong, *J. Phys.: Conf. Ser.*, 2021, **2109**, 012004.
9 H. Pan, Y.-S. Hu and L. Chen, *Energy Environ. Sci.*, 2013, **6**, 2338–2360.
10 S.-W. Kim, D.-H. Seo, X. Ma, G. Ceder and K. Kang, *Adv. Energy Mater.*, 2012, **2**, 710–721.
11 Y. Xu, E. Memarzadeh Lotfabad, H. Wang, B. Farbod, Z. Xu, A. Kohandehghan and D. Mitlin, *Chem. Commun.*, 2013, **49**, 8973.
12 D. Aurbach, *Solid State Ionics*, 2002, **148**, 405–416.
13 L. Wu, D. Bresser, D. Buchholz, G. A. Giffin, C. R. Castro, A. Ochel and S. Passerini, *Adv. Energy Mater.*, 2015, **5**, 1401142.

14 U. Diebold, *Surf. Sci. Rep.*, 2003, **48**, 53–229.
15 D. Deng, M. G. Kim, J. Y. Lee and J. Cho, *Energy Environ. Sci.*, 2009, **2**, 818.
16 S. Liang, X. Wang, Y.-J. Cheng, Y. Xia and P. Müller-Buschbaum, *Energy Stor. Mater.*, 2022, **45**, 201–264.
17 O. Eroglu and H. Kizil, *J. Phys. Chem. Solids*, 2023, **178**, 111352.
18 Y.-X. Wu, S.-F. Liu, R. Lu, C. Liu and Q. Sun, *Ionics*, 2023, **29**, 2723–2733.
19 W. Wang, Y. Liu, X. Wu, J. Wang, L. Fu, Y. Zhu, Y. Wu and X. Liu, *Advanced Materials Technologies*, 2018, **3**, 1800004.
20 J. Patra, S.-C. Wu, I.-C. Leu, C.-C. Yang, R. S. Dhaka, S. Okada, H.-L. Yeh, C.-M. Hsieh, B. K. Chang and J.-K. Chang, *ACS Appl. Energy Mater.*, 2021, **4**, 5738–5746.
21 J. Jamnik and J. Maier, *Chem. Phys.*, 2003, **5**, 5215.
22 K. T. Lee and J. Cho, *Nano Today*, 2011, **6**, 28–41.
23 J.-Y. Shin, D. Samuelis and J. Maier, *Adv. Funct. Mater.*, 2011, **21**, 3464–3472.
24 S. Y. Chae, M. K. Park, S. K. Lee, T. Y. Kim, S. K. Kim and W. I. Lee, *Chem. Mater.*, 2003, **15**, 3326–3331.
25 H.-G. Jung, S. W. Oh, J. Ce, N. Jayaprakash and Y.-K. Sun, *Electrochem. commun.*, 2009, **11**, 756–759.
26 F. Dufour, S. Cassaignon, O. Durupthy, C. Colbeau-Justin and C. Chanéac, *Eur. J. Inorg. Chem.*, 2012, **2012**, 2707–2715.
27 Y. Ge, H. Jiang, J. Zhu, Y. Lu, C. Chen, Y. Hu, Y. Qiu and X. Zhang, *Electrochimica Acta*, 2015, **157**, 142–148.
28 D. Su, S. Dou and G. Wang, *Chem. Mater.*, 2015, **27**, 6022–6029.
29 Y. Yang, X. Ji, M. Jing, H. Hou, Y. Zhu, L. Fang, X. Yang, Q. Chen and C. E. Banks, *J. Mater. Chem. A*, 2015, **3**, 5648–5655.
30 X. Ma, Z. Zhang, J. Tian, B. Xu, Q. Ping and B. Wang, *Funct. Mater. Lett.*, 2018, **11**, 1850021.
31 H. Tao, M. Zhou, K. Wang, S. Cheng and K. Jiang, *Sci Rep*, 2017, **7**, 43895.
32 A. C. Martins, A. L. Cazetta, O. Pezoti, J. R. B. Souza, T. Zhang, E. J. Pilau, T. Asefa and V. C. Almeida, *Ceram. Int.*, 2017, **43**, 4411–4418.
33 K. Olurode, G. M. Neelgund, A. Oki and Z. Luo, *Spectrochim. Acta A Mol. Biomol. Spectrosc.*, 2012, **89**, 333–336.
34 M. Maletić, M. Vukčević, A. Kalijadis, I. Janković-Častvan, A. Dapčević, Z. Laušević and M. Laušević, *Arab. J. Chem.*, 2019, **12**, 4388–4397.
35 C. Coromelci-Pastravanu, M. Ignat, E. Popovici and V. Harabagiu, *J. Hazard. Mater.*, 2014, **278**, 382–390.
36 M. J. Velasco, F. Rubio, J. Rubio and J. L. Oteo, *Spectrosc. Lett.*, 1999, **32**, 289–304.
37 L. Wu, D. Buchholz, D. Bresser, L. Gomes Chagas and S. Passerini, *Journal of Power Sources*, 2014, **251**, 379–385.
38 W. Devina, D. Nam, J. Hwang, C. Chandra, W. Chang and J. Kim, *Electrochimica Acta*, 2019, **321**, 134639.
39 K. Judai, N. Iguchi and Y. Hatakeyama, *J. Chem.*, 2016, **2016**, 1–6.
40 K. Gao, *Phys. B: Condens.*, 2007, **398**, 33–37.
41 A. Orendorz, A. Brodyanski, J. Lösch, L. H. Bai, Z. H. Chen, Y. K. Le, C. Ziegler and H. Gnaser, *Surf. Sci.*, 2007, **601**, 4390–4394.
42 Q. Zhang, H. He, X. Huang, J. Yan, Y. Tang and H. Wang, *J. Chem. Eng.*, 2018, **332**, 57–65.
43 F.-F. Cao, X.-L. Wu, S. Xin, Y.-G. Guo and L.-J. Wan, *J. Phys. Chem. C*, 2010, **114**, 10308–10313.
44 H. He, Q. Gan, H. Wang, G.-L. Xu, X. Zhang, D. Huang, F. Fu, Y. Tang, K. Amine and M. Shao, *Nano Energy*, 2018, **44**, 217–227.
45 Z. Luo, S. Liu, Y. Cai, S. Li, A. Pan and S. Liang, *Energy Technol.*, 2018, **6**, 759–765.
46 O. Beyssac and M. Lazzeri, in *Raman spectroscopy applied to Earth sciences and cultural heritage*, eds. G. Ferraris, J. Dubessy, M.-C. Caumon and F. Rull, European Mineralogical Union, 2012, pp. 415–454.
47 A. Merlen, J. Buijnsters and C. Pardanaud, *Coatings*, 2017, **7**, 153.
48 M. N. Tahir, B. Oschmann, D. Buchholz, X. Dou, I. Lieberwirth, M. Panthöfer, W. Tremel, R. Zentel and S. Passerini, *Adv. Energy Mater.*, 2016, **6**, 1501489.

View Article Online
DOI: 10.1039/D4DT00459K